Applied Geochemistry 87 (2017) 57–70

Contents lists available at ScienceDirect

Applied Geochemistry

journal homepage: www.elsevier.com/locate/apgeochem

Mineral dissolution in porous media: An experimental and modeling study on kinetics, porosity and surface area evolution

Jan Přikryl [a, *], Diwaker Jha [b], Andri Stefánsson [a], Susan Stipp [b]

[a] Institute of Earth Sciences, University of Iceland, Sturlugata 7, 101 Reykjavík, Iceland
[b] Nano-Science Center, Department of Chemistry, University of Copenhagen, Denmark

ARTICLE INFO

Article history:
Received 26 January 2017
Received in revised form
20 April 2017
Accepted 1 May 2017
Available online 4 May 2017

Editorial handling by Prof. M. Kersten

Keywords:
Dissolution
Flow-through experiment
Surface area
Porosity
Porous medium
Tomography
Kinetic model

ABSTRACT

Mineral and rock dissolution was studied experimentally using flow-through reactors and reactive transport modeling. The porous media were forsterite, crystalline basalt, and amorphous basalt, dissolved in HCl solutions at pH ~2.5 and 25 °C. Solution composition, particle surface area, and porosity were determined as a function of travel distance within the reactor and time, using in situ X-ray computed tomography (XMT) and solution chemical composition. The obtained bulk dissolution rates, normalized to the initial geometric surface area, were: log $r_{+,Si}$ −7.59 ± 0.05 for forsterite, −7.64 ± 0.12 for basaltic glass and −8.12 ± 0.24 (mol/m^2/s) for crystalline basalt, at 25 °C and pH ~2.5, similar to those previously obtained using mixed flow reactors and for conditions far from equilibrium. Mineral and rock dissolution resulted in increased porosity and specific surface area of the solids; these changes were not uniformly distributed along the fluid flow path or with time. Similar trends were predicted by reactive transport modeling, however, the exact values of pore volume and surface area were difficult to predict. The results were found to be independent of the method applied in the surface area calculations: either the simple spherical model or the sugar lump model. Also, in the models, stoichiometric mineral dissolution is commonly assumed, but was not observed to occur for either glassy or crystalline basalt. It shows that accurate prediction capabilities of simple reactive transport modeling may be limited for calculating pore volume, mineral and rock surface area changes, and pore fluid chemistry with time and along flow paths. These, in turn, are key parameters in determining dissolution rates, overall chemical mass movement in the system, and fluid flow paths and velocities.

1. Introduction

Weathering and alteration of rocks by water-rock interaction play a key role in many geochemical cycles, for example in forming landscapes and soils (Brantley et al., 2008), in the effectiveness of carbon capture and storage (e.g., McGrail et al., 2006; Gíslason and Oelkers, 2014), in acid mine drainage, and in the transport of toxic elements (e.g. Akcil and Koldas, 2006; Gandy et al., 2007).

The initial step of water-rock interaction in porous media is dissolution of primary minerals by fluid, usually water, resulting in dissolved solutes and formation of secondary minerals. Commonly, the rate of the overall water-rock interaction is quantified by change in solution composition as a function of time. Most common are dissolution experiments (e.g., Pokrovsky and Schott, 2000; Oelkers and Gíslason, 2001) but rates of secondary mineral formation have also been determined (e.g., Nagy et al., 1991; Saldi et al., 2009). In porous rocks, mineral dissolution and formation of secondary minerals may also cause changes in pore volume, permeability and mineral surface area, however, these effects have received less attention (e.g., Kieffer et al., 1999; Colón et al., 2004).

Dissolution rates determined from experiments are commonly higher than those determined from field studies (e.g. White and Brantley, 2003). The causes can be many. Dissolution rates are influenced by available mineral surface area and the availability and transport of water to and from those surfaces. The surfaces of natural minerals may be previously weathered compared with those used in experiments, this affecting the measured dissolution rates. Moreover, mineral surface area may vary and change during progressive water-rock interaction and weathering and water transport are influenced by the porosity and permeability of the rocks. In recent years, advances in computed tomography (CT) have provided new insight into water-rock interaction in porous media,

* Corresponding author.
E-mail address: jap5@hi.is (J. Přikryl).

http://dx.doi.org/10.1016/j.apgeochem.2017.05.004
0883-2927/

particularly the changes in porosity and particle surface area (e.g., Noiriel et al., 2004, 2009; 2012; Noiriel, 2015; Luquot and Gouze, 2009; Gouze and Luquot, 2011; Cnudde and Boone, 2013; Molins et al., 2014). These studies have demonstrated that dissolution and precipitation kinetics can be influenced by fluid transport and availability of surface area and that surface area and porosity usually change as a function of flow path and progressive water-rock interaction.

This study focused on water-rock interaction and mineral dissolution in porous media. Flow-through experiments were conducted where the dissolution of single and multiphase, unconsolidated porous media, with crystalline or amorphous material, was investigated. The progress of the reaction was followed by in situ imaging and by chemical analysis, which allowed changes in local porosity and surface area to be determined along the flow path, as a function of time. The chemical composition data were used to determine dissolution rates. The experimental data were compared with results from reactive transport modeling, to validate prediction capabilities of such model calculations for solution composition and changes in porosity and mineral surface area.

2. Methods

2.1. Experimental details

Three materials were used for the experiments: basaltic glass (BG) as an amorphous single phase, crystalline basalt (XB) as a crystalline multiphase and forsterite (FO) representing a crystalline single phase system. The composition of the basaltic glass was close to that of mid-ocean ridge basalt (MORB) and was collected from Stapafell, SW Iceland. The material has been described previously (e.g., Oelkers and Gíslason, 2001; Gíslason and Oelkers, 2003; Gysi and Stefánsson, 2012a,b,c; Stockmann et al., 2011; Galeczka et al., 2014). The bulk composition of the crystalline basalt was similar to the basaltic glass and was collected at the same locality. The mineralogy and petrology of the material have previously been reported by Gudbrandsson et al. (2011). The forsterite ($Mg_{1.86}Fe_{0.14}SiO_4$) used in this study was collected in Gusdal quarry, in the Almklovdalen peridotite massif, situated in the Western Gneiss Region, Norway (Brueckner et al., 2010).

The solid materials were broken in a jaw crusher, then ground in an automatic agate mortar and dry sieved to obtain the 125–250 μm size fraction. We used gravitational settling in deionized ultrapure water and the water further served to remove the ultrafine particles. The material was rinsed with deionized water and acetone in an ultrasonic bath and dried in an oven at 40 °C. A summary of the chemical and physical properties of the starting material is given in Table 1 and SEM images of the fresh material are shown in Fig. 1. The specific geometric surface area of the starting materials was determined as (Tester et al., 1994),

$$A_{geo} = \frac{6}{de * \rho} \quad (1)$$

the constant, 6, is a shape factor, used for grains that are spherical and smooth. The effective particle diameter is denoted *d*e, and ρ stands for the density of the material. The BET specific surface area of cleaned and dried starting materials was determined by six point nitrogen adsorption, using a Quantachrome Gas Sorption system.

The dissolution experiments were conducted at 25 °C using a flow-through reactor system, consisting of an inlet solution, a peristaltic pump, a vertically placed reaction vessel and an outlet tube. The cylindrical Teflon reactor had a volume of 8.80 cm^3, length (l) of 11.2 cm and internal diameter (Ø) of 0.5 cm. The reactors had thin walls (3 mm) for in situ X-ray microtomography (XMT) measurements as a function of reaction time and distance along the flow path within the reactor. Prior to the experiments, the reactor was loaded with one of the solid materials, in suspension, to optimize homogeneous particle distribution and to avoid preferential channeling.

The inlet solutions were made from HCl (37% Sigma-Aldrich) and deionized water to form 8.44–8.68 mmol/kg HCl with pH of 2.10–2.11. The solutions were pumped at a constant flow rate (0.5 ml/min) through the columns. The solid material and the inlet and outlet solution compositions were determined during the experimental runs. A schematic figure of the experimental setup is presented in Fig. 2, together with an example of 3D XMT images of the material before and after dissolution, taken in situ. The experimental conditions are summarized in Table 2.

2.2. Solid material analysis

The solid materials were analyzed at the beginning and at the end of the experiments. Scanning electron microscopy (SEM, HITACHI TM-3000) showed the morphology of the grains. Images of gold coated samples were taken at an accelerating voltage of 15 kV, at a range of magnifications. The chemical composition of the fresh material was determined using an electron microprobe (JEOL JXA-8200 Superprobe), at an accelerating voltage of 15 kV, a beam current of 15 nA, and a beam size of 1–5 μm.

2.3. Solution composition and dissolution rates

Solution samples for chemical analysis were collected at the

Table 1
Physical and chemical properties of the starting solid material used in the experiments.

	Basaltic glass (BG)	Crystalline basalt (XB)	Forsterite (FO)
Chemical composition	$Na_{0.081}K_{0.008}Mg_{0.282}Ca_{0.263}Fe_{0.171}Al_{0.358}SiO_{3.297}$[a]	18% fo 37% cpx 45% plag[b] fo - $Mg_{1.68}Fe_{0.32}SiO_4$[b] cpx - $Ca_{0.4175}Mg_{0.399}Fe_{0.209}Si_{0.973}O_3$[b] plag - $Ca_{0.67}Na_{0.33}Al_{1.55}Si_{2.416}O_8$[b]	$Mg_{1.86}Fe_{0.14}SiO_4$
Grain size	125–250 μm	125–250 μm	125–250 μm
Material (g)	12.96	13.61	17.41
Geometric surface area (A_{geo}) (m^2/g)	0.0303	0.0284	0.0263
BET surface area (A_{BET}) (m^2/g) literature	1.533[c]	0.812[b]	0.088[d]
BET surface area (A_{BET}) (m^2/g) this study (N_2)	5.274	0.924	0.079
X-ray microtomography surface area (A_{XMT}) (m^2/g)	0.0118	0.0127	0.0137
X-ray microtomography porosity (ϕ_{XMT}) (%)	49.53	51.74	41.90

[a] Oelkers and Gíslason (2001).
[b] Gudbrandsson et al. (2011). The composition of cpx has been simplified to exclude Al and to be consistent with the mineral solubilities.
[c] Aradóttir et al. (2013).
[d] Giammar et al. (2005).

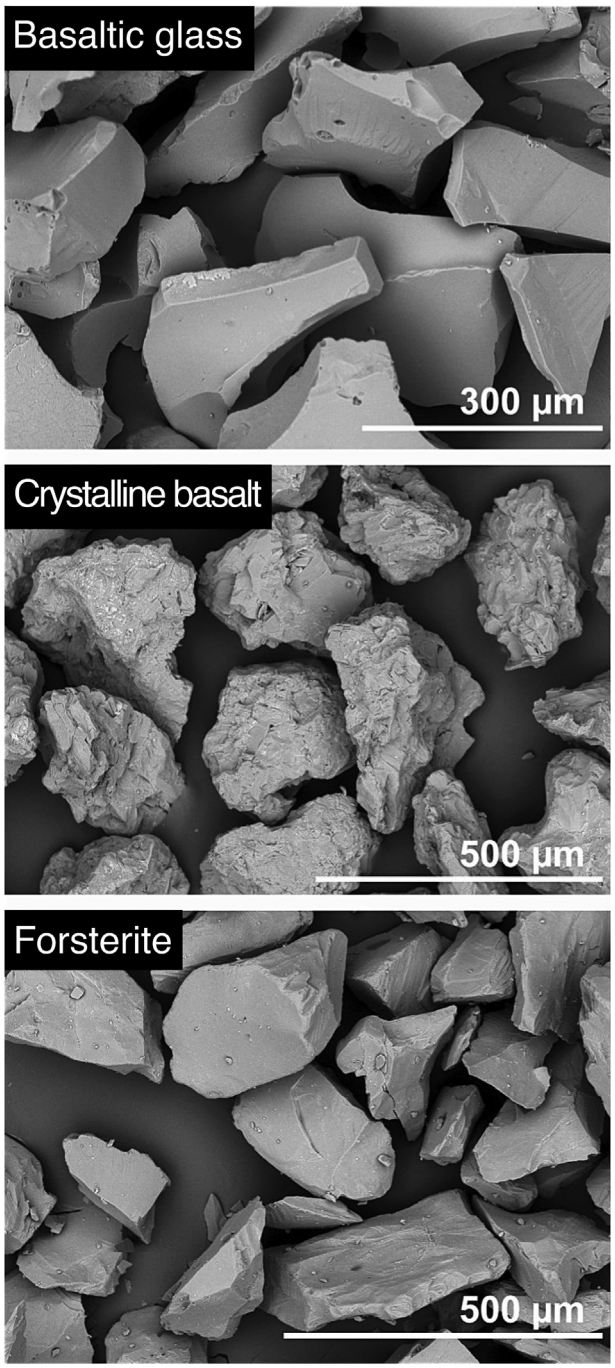

Fig. 1. SEM images of unreacted starting materials.

inlet and outlet of the flow-through reactor. The solutions were filtered through 0.2 μm cellulose acetate filters. Two aliquots were collected, one for pH determination with a glass electrode (Cole-Parmer), that was calibrated against NBS standard buffers, and another that was acidified with 1% HNO_3 (Merck Suprapur®) for major element analysis (Si, Na, K, Ca, Mg, Fe, Al, B and Cl) by ICP-OES (Spectro Ciros Vision). The analytical uncertainty, based on repeated analysis of an internal standard (GYG13) at the 95% confidence level, ranged from 0.3 to 4.8% for the various elements. The absolute error of the pH measurements was estimated to be ±0.05 pH units. The results were obtained by comparing the measured pH of several solutions using an electrode calibrated against the standard buffers as well as with a more rigorous standard addition calibration with acid-base titration and determination of standard potential, Nernstian slope, and acid and alkaline liquid junction potentials.

Based on the difference in chemical composition of the inlet and outlet solutions, the forward dissolution rate (r_{+i}) was calculated from the expression,

$$r_{+i} = \frac{\Delta m_i q}{A} \tag{2}$$

where Δm_i represents the concentration difference between the inlet and outlet solutions for the i-th element, Δm_i was divided by stoichiometric coefficient of the i-th element in the case of Mg, and q denotes flow rate. The surface area, A, was assumed to be the initial geometric surface area of the material inside the reactor or the surface area determined from the 3D XMT images as a function of time. The dissolution rates were derived using the Si and Mg concentrations.

Exact mass of residual material in the reactor for XMT normalized dissolution rate was obtained from the mass of dissolved material ($\Delta M(t)$) calculated from the following equation:

$$\Delta M(t) = \sum_{i=1}^{n} m_i(t) \text{ where } m_i(t) = \int_0^t (c_{i,\,in} - c_{i,\,out}(t)) q(t)\ dt \tag{3}$$

with $c_{i,\,in}$ and $c_{i,\,out}$ as the concentrations of the i-th cation (mmol/kg) in the inlet and outlet fluids respectively, q the flow-rate (L/s) and m_i the total moles of cation released from the sample at time t. The total mass of cations was converted to mass of respective oxides (SiO_2, Al_2O_3, CaO, MgO, FeO).

2.4. X-ray microtomography, calculation of porosity and specific surface area

Tomography measurements were made using a Phoenix Nanotom S X-ray microCT system (General Electric Measurement and Control) situated at Innovation Center Iceland, Reykjavík, at a source current of 140 μA, a source voltage of 120 kV and a sampling distance of 7.83–8.83 μm. Measurements were made on the original material, prior to the experiments, and after 2 and 4 weeks of dissolution, for the inlet (z = 20–27 ± 2 mm) and outlet portions of the reactor (z = 100–107 ± 2 mm). Two phase (solid and fluid) reconstructed 3D tomography data was processed as follows: 1) Each voxel, $I_{(x,y,z)}$ with intensity value greater than $(\mu_{(I)} + 3\sigma_{(I)})$ was replaced by $(\mu_{(I)} + 3\sigma_{(I)})$. Here, $\mu_{(I)}$ is the mean intensity value and $\sigma_{(I)}$, the standard deviation of the tomogram's voxel values. This removed any outlier patch of pixels. 2) Noise level was estimated following Liu et al. (2013). 3) Bilateral filtering was performed using the noise level parameter obtained in Step 2 (Tomasi and Manduchi, 1998). 4) At this point, voxels representing solid and fluid were segmented by setting a threshold level obtained by Otsu method (Otsu, 1979). These steps improved the segmentation by minimizing false pore matrix indicators (Jha et al., 2014). The intensity histograms show a clear bimodal distribution after the processing steps, which allows a reliable and automatic selection of threshold levels (Fig. 3). We calculated the digital surface area (pixel^2) of the segmented binary data by counting marching cube surface values in it. Total digital surface area was converted to physical surface area (in m^2) by multiplying it with the area of a voxel's face. The porosity, ϕ, was given by $\frac{V-V_s}{V}$, where V is the total volume of voxels in the tomogram and V_s is the total solid phase

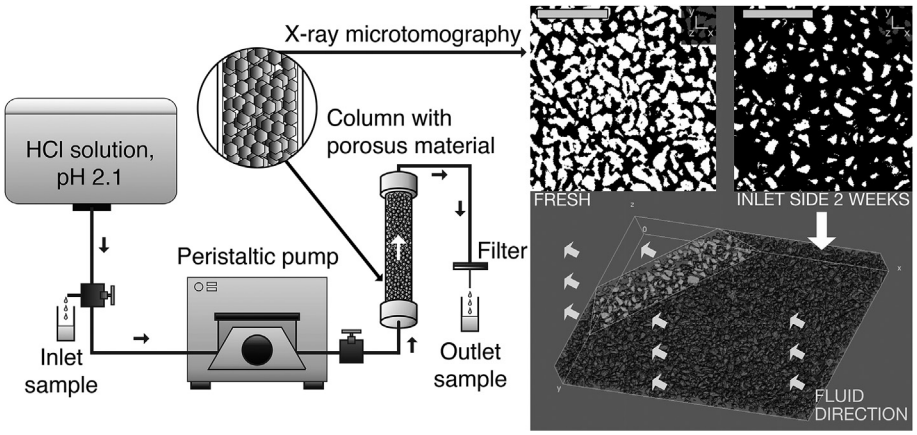

Fig. 2. A schematic diagram for the X-ray microtomography setup, consisting of inlet solution, peristaltic pump, flow-through reactor and outlet sampling port. The reactor was made of Teflon with a wall thickness of 3 mm to allow in situ X-ray scanning. Examples of raw, binarized data are presented, with a 3 dimensional reconstruction of the porous media. The scale bar on the tomogram slices is 600 μm.

Table 2
Summary of the parameters for the experiments.

	Basaltic glass (BG)	Crystalline basalt (XB)	Forsterite (FO)
Exp. #	BG 0-9	XB 0-11	FO 0-10
Temperature (°C)	25	25	25
Duration (days)	29	30	30
Flow rate (ml/min)	0.48–0.53	0.41–0.54	0.40–0.54
Solution compostion HCl (mmol/kg)	8.40–8.60	8.25–8.74	8.11–8.74
Solution pH at 25 °C	2.11–2.85	2.10–2.34	2.10–2.86
Solid material SEM analysis Exp. #	0, 9	0, 11	0, 10
Porosity analysis Exp. #	0, 5, 9	0, 6, 11	0, 7, 10
Surface area analysis Exp.#	0, 5, 9	0, 6, 11	0, 7, 10

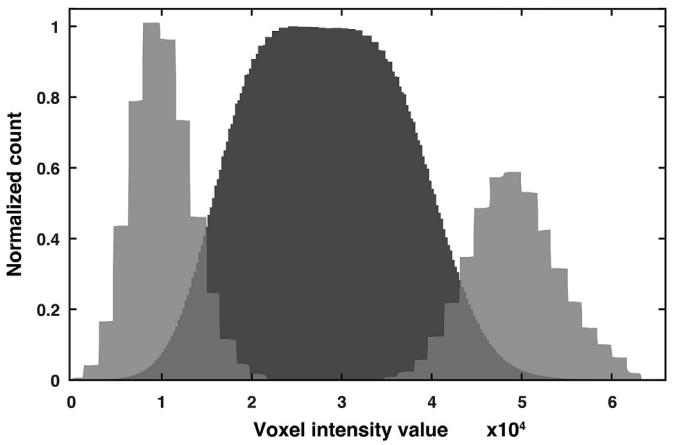

Fig. 3. Intensity histogram of the tomogram voxels before (black) and after (gray) processing steps, which allow automatic determination of threshold level.

voxel count. The mass (g) of the solid material was obtained from V_s and the material density, ρ. This consequently allowed us to calculate specific surface area in commonly used units (m^2/g). In order to calculate the tomographic surface normalized dissolution rates, the average surface area, $\overline{X}$, over all of the solid was calculated as the arithmetic mean,

$$\overline{X} = \frac{1}{n}\sum_{i=1}^{n} X_i \tag{4}$$

where n represents the set of sample and X_i, the specific surface area of samples. Consequently average surface area, $\overline{X}$, was multiplied with the residual mass of material to obtain total surface area.

2.5. Reactive transport modeling

Reactive transport modeling was conducted using the PHREEQC program (Parkhurst and Appelo, 2013). The reactor was divided into 10 reactive cells to track reaction progress as a function of column distance, with a total 52 to $62 \cdot 10^3$ transport calculation steps per cell to calculate 1 month of experimental duration. This number of transport shifts depended on the initial pore volume and corresponding solution refill rate; the time step associated with each shift was close to 1 minute. 1D advective-dispersive-reactive transport of the solution was determined using the forward flow direction from cell 1 up to cell 10 to mimic experimental behavior (Appelo and Postma, 2005). Dispersivity in each cell (10% of travelled distance) was corrected for the total length of the cell and we assumed no diffusion.

The rate of dissolution was calculated using the transition state theory for the i-th solid phase,

$$r_{+i} = A_i \sum_i \left(k_{T,i} \prod_j a_j^n \right) (1 - SI_i) \tag{5}$$

where A represents the surface area, k_T represents the kinetic rate constant at a given pH and temperature, and $\prod_j a_j^n$ represents the activity expression for the j-th dissolved aqueous species in the solution, to the power of the reaction order of species j, n.

The saturation index, SI, was calculated from,

$$SI_i = Q_i/K_i \quad (6)$$

where Q denotes the reaction quotient of the dissolution reaction and K, the respective equilibrium solubility constant.

Dissolution rates and solubility data used in this study are listed in Table 3. These were taken from dissolution rate studies reported by Gíslason and Oelkers (2003), Palandri and Kharaka (2004), Olsen and Rimstidt (2008), and Gudbrandsson et al. (2014). The thermodynamic data for aqueous species and the minerals used to calculate the mineral solubilities were taken from by Phillips et al. (1988), Shock and Helgeson (1988), Cox et al. (1989), Shock et al. (1997), Arnórsson and Andrésdóttir (1999), Arnórsson and Stefánsson (1999), Gunnarsson and Arnórsson (2000), Stefánsson (2001), and Aradóttir et al. (2012).

The pore volume or porosity, ϕ, was calculated from the volume difference between the empty experimental reactor and the volume of the solid material in the reactor. The volume of solid was determined from the mass of material divided by its density.

The total surface area of the grains, A, was determined in two ways, first, by assuming spherical grains and homogeneous dissolution of the solid particles with time, and second, using the sugar lump model (Noiriel et al., 2009), where material is dissociated into smaller grains, which increased the surface area. In the spherical dissolution model, the surface area of the dissolving phases was calculated from the initial surface area, A_0, and the ratio of the initial number of moles of the solid, m_0, and the number of moles remaining, as a function of time, m_t, assuming the grains to be spherical, hence a factor of 2/3,

$$A = \varsigma_i A_0 \left(\frac{m_t}{m_0}\right)^{2/3} \quad (7)$$

In this model, total surface area does not increase with dissolution progress. However, in the sugar lump model, dissolution can generate extra surface initially and then decrease it,

$$A = \varsigma_i \left(A_0 + A_m \left(1 - \left(\frac{m_t}{m_0}\right)^{n_1}\right)^{n_2}\right)\left(\frac{m_t}{m_0}\right)^{n_3} \quad (8)$$

where A_m represents the maximum surface area, which is given by the sum of the surface area for all of the individual particles. $n_{1,2,3}$ are empirical coefficients that depend on the geometry of the aggregate. Coefficient n_3 is equal to 2/3, assuming spherical grains. In addition to the sugar lump model, the coefficient ς_i represents the fraction of reactive surface area of the solids. Its value can range from 0 to 1, where 0 represents the case where none of the surface is reactive and 1, where all of the surface reacts. Here, we have assumed ς_i to be 1 but the reactive surface area could be only a part of the total surface area (e.g., Brantley and Mellott, 2000; Colón et al., 2004; Aagaard and Helgeson, 1982; Helgeson et al., 1984), and it could vary greatly over long periods of water-rock interaction. This would cause dissolution rates to change significantly (e.g., Lichtner, 1996; White and Brantley, 2003; Luquot and Gouze, 2009; Noiriel et al., 2004).

3. Results

3.1. Solution composition

The chemical composition of the inlet and outlet solutions is presented in Table 4. The concentration of the inlet solution for all experiments was similar, between 8.44 and 8.68 mmol/kg HCl, pH of 2.10–2.11, and the concentration of other elements was below detection. The outflow solution pH was similar from all solid

Table 3
Thermodynamic and kinetic data used for the kinetic reaction path simulations. Kinetic constants were recalculated for geometric surface area.

Solid	Symbol	Simulation	Mineral compostion	Dissolution reaction	log $K_{25°C}$	log $k_{i\ 25°C}$ (mol/m^2/sec)	$r_{\pm} = A_{geo}\ k\ (1\text{-}SI_i^n)$
Basaltic glass	BG	BG	$Na_{0.081}K_{0.008}Mg_{0.282}Ca_{0.263}Fe_{0.171}Al_{0.358}SiO_{3.297}$[a]	$Na_{0.081}K_{0.008}Mg_{0.282}Ca_{0.263}Fe_{0.171}Al_{0.358}SiO_{3.297} + 1.162H^+ + 2.135H_2O = 0.081Na^+ + 0.008K^+ + 0.263Ca^{2+} + 0.282Mg^{2+} + 0.171Fe^{2+} + 0.358Al(OH)_4^- + H_4SiO_4$	2.92[d]	[g] 8.557E − 07$(a_{H+}^3/a_{H_2O})^{1/3}$	$A\ k\ (1\text{-}SI)$
Crystalline basalt	Cpx	XB	$Ca_{0.415}Mg_{0.399}Fe_{0.209}Si_{0.9735}O_3$[b]	$Ca_{0.415}Mg_{0.399}Fe_{0.209}Si_{0.9735}O_3 + 2.106H^+ + 0.894H_2O = 0.415Ca^{2+} + 0.399Mg^{2+} + 0.209Fe^{2+} + 0.9735H_4SiO_4$	10.05[e]	[h] −6.82	$A\ k_a\ a_{H+}^{0.7}\ (1\text{-}SI)$
			$En_{0.11}Fs_{0.06}Di_{0.55}Hed_{0.28}$				
	Plag	XB	$Ca_{0.674}Na_{0.338}Al_{1.550}Si_{2.416}O_8$[b]	$Na_{0.33}Ca_{0.67}Al_{1.55}Si_{2.416}O_8 + 7.864H_2O + 0.136\ H^+ = 0.33Na^+ + 0.67Ca^{2+} + 1.55Al(OH)_4^- + 2.416H_4SiO_4$	18.61[f]	[i] $10^{(0.33\ \log(a_{H+}^3/a_{W})-12.46)}$ 10000	$A\ k\ (1\text{-}SI)$
			$An_{67}Ab_{33}$				
	Fo	XB	$Mg_{1.68}Fe_{0.32}SiO_4$[b]	$Mg_{1.68}Fe_{0.32}SiO_4 + 4H^+ = 1.68Mg^{2+} + 0.32Fe^{2+} + H_4SiO_4$	27.38[e]	[j] −7.54	$A\ k\ (1\text{-}SI)$
			$Fo_{84}Fa_{16}$				
Forsterite	Fo93	FO	$Mg_{1.86}Fe_{0.14}SiO_4$[c]	$Mg_{1.86}Fe_{0.14}SiO_4 + 4H^+ = 1.86Mg^{2+} + 0.14Fe^{2+} + H_4SiO_4$	28.43[e]	[j] −7.54	$A\ k\ (1\text{-}SI)$
			$Fo_{93}Fa_7$				

[a] Oelkers and Gíslason (2001).
[b] Gudbrandsson et al. (2011).
[c] This study.
[d] Calculated using the approach of Techer et al. (2001) with dissolution equilibrium constants presented by Phillips et al. (1988) and Aradóttir et al. (2012).
[e] Stefánsson (2001).
[f] Arnórsson and Stefánsson (1999).
[g] From Gíslason and Oelkers (2003).
[h] Augite from Palandri and Kharaka (2004).
[i] Gudbrandsson et al. (2014).
[j] From Olsen and Rimstidt (2008).

Table 4
Chemical composition of the solutions sampled at the column outlet.

Exp. #	Time	Flow rate	pH/25 °C	Si	Na	K	Ca	Mg	Fe	Al	Cl
	Days	ml/min		mmol/kg	mmol/kg	mmol/kg	mmol/kg	mmol/kg	mmol/kg	mmol/kg	mmol/kg
Basaltic glass											
BG inlet			2.11	0.010	<0.04	<0.02	<0.001	<0.001	0.0006	0.002	8.44
BG 1 outlet	4	0.51	2.92	1.32	0.248	0.021	0.760	0.731	0.504	0.981	8.49
BG 2 outlet	6	0.5	2.85	1.33	0.239	0.020	0.734	0.705	0.502	0.940	8.48
BG 3 outlet	8	0.5	2.85	1.37	0.234	0.021	0.737	0.707	0.485	0.927	8.43
BG 4 outlet	10	0.53	2.73	1.39	0.220	0.028	0.685	0.663	0.461	0.864	8.49
BG 5 outlet	15	0.5	2.25	0.64	0.097	<0.02	0.241	0.257	0.193	0.314	8.60
BG 6 outlet	20	0.53	2.36	0.80	0.137	0.059	0.382	0.394	0.269	0.488	8.48
BG 7 outlet	22	0.48	2.52	1.09	0.201	<0.02	0.547	0.554	0.366	0.678	8.51
BG 8 outlet	25	0.48	2.66	1.35	0.208	<0.02	0.640	0.639	0.422	0.792	8.40
BG 9 outlet	29	0.48	2.62	1.38	0.199	0.020	0.622	0.625	0.417	0.795	8.56
Crystalline basalt											
XB inlet			2.10	0.020	<0.04	<0.02	<0.001	0.004	0.003	0.004	8.68
XB 1 outlet	1	0.47	2.24	0.438	0.047	<0.02	0.188	0.418	0.277	0.145	8.59
XB 2 outlet	3	0.44	2.33	0.814	0.049	<0.02	0.097	0.952	0.490	0.137	8.74
XB 3 outlet	6	0.44	2.34	0.804	0.047	<0.02	0.089	0.962	0.467	0.146	8.60
XB 4 outlet	9	0.44	2.32	0.706	0.1833	<0.02	0.091	0.820	0.392	0.165	8.54
XB 5 outlet	11	0.45	2.28	0.589	0.066	<0.02	0.093	0.628	0.303	0.182	8.42
XB 6 outlet	13	0.51	2.23	0.433	0.043	<0.02	0.086	0.456	0.213	0.176	8.56
XB 7 outlet	16	0.51	2.21	0.320	0.044	<0.02	0.086	0.306	0.133	0.186	8.43
XB 8 outlet	20	0.54	2.19	0.255	0.043	<0.02	0.089	0.213	0.075	0.193	8.38
XB 9 outlet	25	0.41	2.20	0.244	<0.04	<0.02	0.097	0.181	0.056	0.215	8.25
XB 10 outlet	28	0.45	2.18	0.205	<0.04	<0.02	0.090	0.139	0.041	0.199	8.37
XB 11 outlet	30	0.54	2.17	0.171	<0.04	<0.02	0.081	0.102	0.030	0.178	8.36
Forsterite											
FO inlet			2.10	0.006	<0.04	<0.02	<0.001	<0.001	0.0003	<0.001	8.68
FO 1 outlet	1	0.47	2.75	1.76	<0.04	<0.02	0.002	3.12	0.229	0.003	8.72
FO 2 outlet	3	0.47	2.64	1.69	<0.04	<0.02	0.001	2.87	0.210	0.002	8.74
FO 3 outlet	6	0.47	2.62	1.54	<0.04	<0.02	<0.001	2.77	0.197	0.002	8.62
FO 4 outlet	9	0.47	2.56	1.46	<0.04	<0.02	0.002	2.57	0.186	0.003	8.59
FO 5 outlet	11	0.46	2.86	1.69	<0.04	<0.02	<0.001	3.05	0.212	0.002	8.11
FO 6 outlet	13	0.53	2.54	1.35	<0.04	<0.02	<0.001	2.37	0.170	0.002	8.31
FO 7 outlet	16	0.51	2.48	1.25	<0.04	<0.02	<0.001	2.19	0.164	0.001	8.37
FO 8 outlet	20	0.54	2.52	1.35	<0.04	<0.02	<0.001	2.39	0.173	0.001	8.53
FO 9 outlet	28	0.42	2.56	1.44	<0.04	<0.02	<0.001	2.50	0.189	0.018	8.52
FO 10 outlet	30	0.40	2.60	1.50	<0.04	<0.02	<0.001	2.64	0.192	0.002	8.52
2σ [a]				0.01	0.05	0.01	0.001	0.0002	0.0003	0.0006	0.05

[a] Analytical uncertainity based on repeated analysis of the reference sample (GYG13).

materials: for basaltic glass, in the range of 2.25–2.92, for crystalline basalt, in the range of 2.17–2.30, and for forsterite, in the range of 2.48–2.86 (Fig. 4). For the output solutions from the crystalline basalt and forsterite experiments, the concentrations of the dissolved elements reached steady state within 10–15 days. For the basaltic glass, outflow solution concentration was relatively constant during the entire experiment.

The reaction stoichiometry can be studied by comparing element ratios in the solutions with those in the bulk solid. For basaltic glass dissolution, the element mole ratios in the outlet solutions after 10 days were Si/Mg = 2.15 ± 0.19, Si/Ca = 2.19 ± 0.25 and Mg/Ca = 0.99 ± 0.03. The corresponding ratios for the initial basaltic glass were 3.55, 3.80 and 0.93, suggesting non-stoichiometric dissolution under acid conditions with respect to Ca and Mg relative to Si. The element ratio in the outlet solution for forsterite was Si/Mg = 0.57 ± 0.01, close to the corresponding mineral ratio, 0.54, indicating stoichiometric dissolution of forsterite. For crystalline basalt, the elemental ratios in the outlet solutions were Si/Mg = 1.35 ± 0.24, Si/Ca = 2.70 ± 0.64 and Mg/Ca = 2.13 ± 0.91, compared with the corresponding bulk crystalline basalt ratios, 3.62, 3.47 and 1.01, respectively, indicating non-stoichiometric dissolution.

3.2. Solid product

The changes in solid surface properties, as a function of distance within the column and time, are shown in Fig. 5. Two features were observed. First, with increasing reaction time, dissolution features became progressively more obvious. This applied for all of the solids. Particle edges were covered by etch pits up to ~20 μm in diameter, which intercepted in some cases and formed corrosion troughs up to ~100 μm in length. Some amorphous basaltic glass grains developed networks of interconnected fractures all over their surfaces, forming flakes (~10–30 μm wide). Such features are caused by preferential dissolution along weaker planes or areas of the glass particles: effects of grain drying and spalling of an altered layer that precipitated on the surface (Gíslason and Oelkers, 2003). Second, dissolution features were unevenly distributed in the column. Deeper etch pits and more extensive dissolution channeling were observed near the inlet of the column than near the outlet. For glass, the powder on inlet side, within the first 1 cm, even lost its black color and appeared mostly white. This indicated extensive dissolution at the inlet, where fresh solution came into contact with the solid. This was accompanied by a slight increase in pH through the rest of the column and slower dissolution toward the outlet.

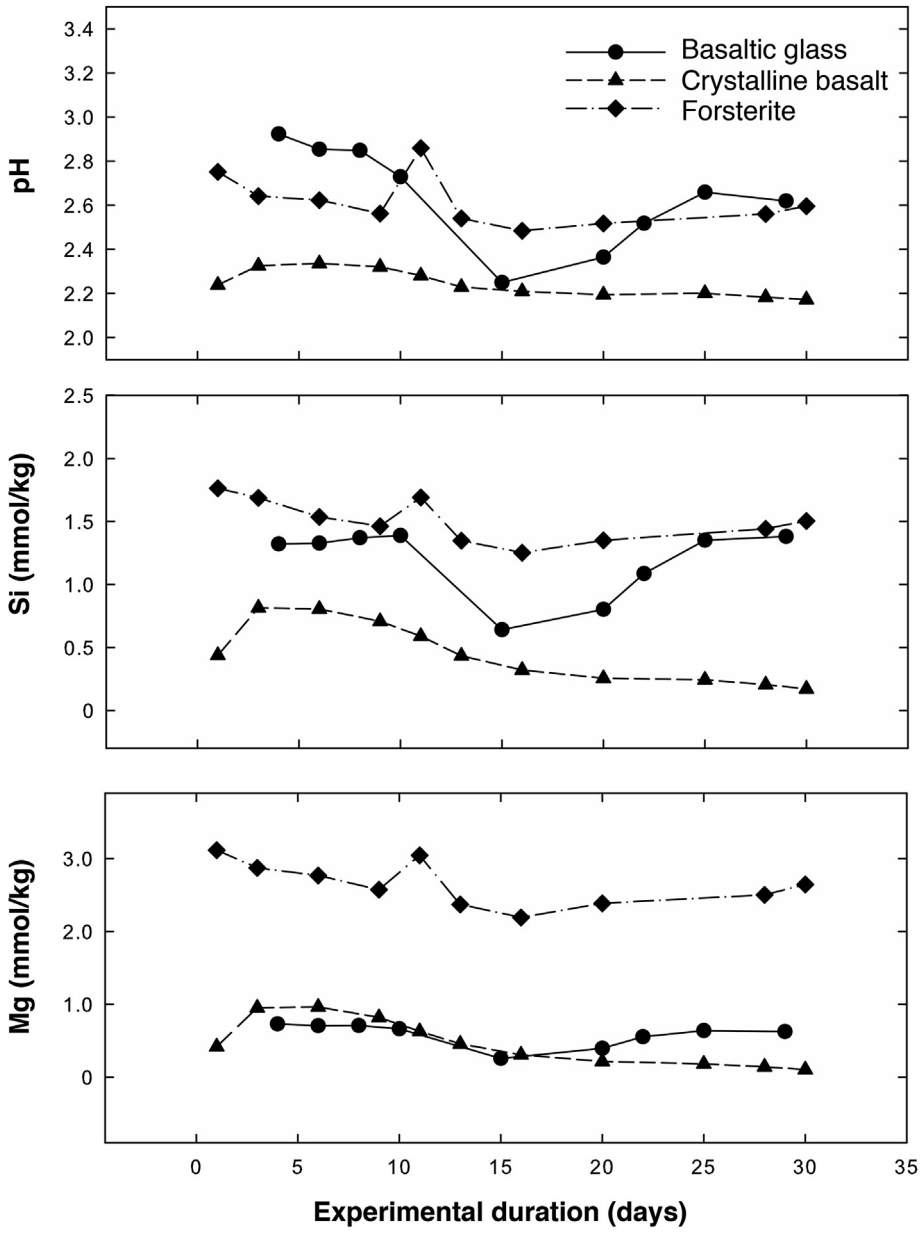

Fig. 4. The composition (pH, Si and Mg) in the outlet solution as a function of time.

3.3. X-ray microtomography

The results derived from X-ray microtomography, i.e. grain size, porosity, ϕ, and surface area, A, for the initial and the reacted material as a function of experiment duration are listed in Table 5.

The grain size distributions for the fresh and reacted material are shown in Fig. 6. There are two characteristic features. First, there was a considerable range in grain size for all of the solids. Although we used the sieved portion that was between 125 and 250 μm, the actual particles ranged from ~50 to ~200 μm, with initial distribution skewed towards the smaller grain size. Second, the median grain size decreased with increasing experiment duration for amorphous and crystalline basalt at the inlet side of the flow-through reactors but increased for forsterite. For basaltic glass, the median value for grain size decreased in the inlet of the reactor, from 103 (±39) μm to 79 (±40) μm after 4 weeks, while the outlet grain size remained relatively constant at 103–97 (±39–37) μm for the first two weeks, followed by a decrease to 77 (±32) μm at the end of the experiment. The trend for crystalline basalt was similar, with a decrease in the inlet grain size from 96 to 90 (±31–33) μm in 4 weeks, whereas the outlet grain size decreased from 96 to 88 (±31) μm throughout the experiment. For forsterite, the grain size did not change significantly at 2 weeks from 71 (±31) to 77 (±32–34) μm, either at the inlet and or the outlet, but at 4 weeks was 80 (±33) μm at the inlet and 64 (±27) μm at the outlet.

The specific surface area of all solids increased during the experiments. These changes were minor for forsterite and crystalline basalts (~7–13% ±5–6 increase in 4 weeks), whereas the specific surface area of basaltic glass changed considerably (up to 43% ± 5 in 4 weeks).

A similar trend was observed for porosity. It increased with experiment duration for all solids. For crystalline basalt and forsterite, these changes were minor, up to 6% ±5–6 increase, whereas the porosity for basaltic glass changed considerably, up to an

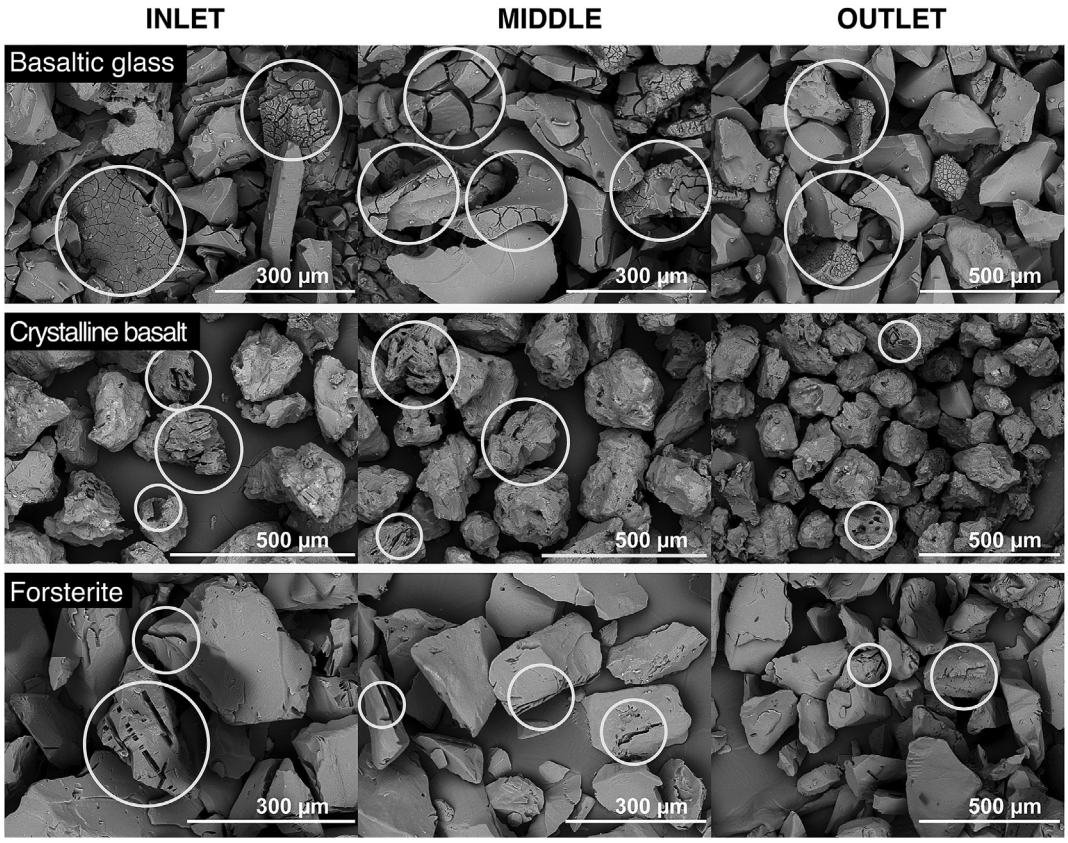

Fig. 5. SEM images of the solids after 4 weeks of reaction from the inlet, middle and outlet of the flow-through reactors. Etch pits and fractures on the reacted material were probably caused by preferential dissolution on weak areas or along weaker planes. Dissolution features are more dominant near the inlet, which indicates more extensive dissolution, where the pH of the fresh solution is lower. During passage through the column, reaction increases pH and the dissolution rate decreases toward the outlet.

Table 5
The measured porosity, ϕ, and surface area, A, determined using X-ray microtomography, XMT.

Exp. #	Time Days	Grain size median µm	ϕ_{XMT} %	A_{XMT} m^2/g
Basaltic glass				
BG inital	0	103	50	0.012
BG 5 inlet	15	78	83	0.020
BG 5 outlet	15	97	46	0.013
BG 9 inlet	29	79	86	0.021
BG 9 outlet	29	77	52	0.018
Crystalline basalt				
XB inital	0	96	52	0.013
XB 6 inlet	13	92	56	0.014
XB 6 outlet	13	92	53	0.013
XB 11 inlet	30	58	58	0.014
XB 11 outlet	30	88	56	0.015
Forsterite				
FO initial	0	71	42	0.014
FO 7 inlet	16	77	43	0.013
FO 7 outlet	16	77	44	0.013
FO 10 inlet	30	80	44	0.013
FO 10 outlet	30	64	46	0.015

Cumulative error is estimated to be ±5% for BG, XB and ±6% for FO.

increase of ~42% ± 5. The change in porosity was not evenly distributed within the reaction column. For all solid types, the difference was greater near the inlet. Porosity increased as grain size decreased and specific surface area increased, in all cases.

These observations demonstrate that dissolution along a flow path resulted in progressive changes in grain size, which led to changes in surface area and pore volume. These changes were dependent on the type of solid.

4. Discussion

4.1. Dissolution rates

The forward dissolution rates were calculated from the difference in solution composition at the inlet and the outlet side of the flow-through reactor, the flow rate and surface area of the solids (Eqn. (2)). The resulting rates with respect to Si and Mg are listed in Table 6 and shown in Fig. 7. For forsterite, the calculated dissolution rates derived from geometric surface area are systematically lower than those calculated from the surface area derived from X-ray microtomography images. The difference was ~0.3 log mol/m^2/s units. Dissolution rates determined from Si and Mg were equivalent to those previously reported by Olsen and Rimstidt (2008) at the same pH and temperature. The Si rates obtained in this study are comparable to those reported by Rimstidt et al. (2012) from a compilation of available literature data but somewhat lower than the rates reported by Oelkers (2001), Golubev et al. (2005) and Pokrovsky and Schott (2000) (Table 7). Rimstidt et al. (2012) concluded that there was a negligible difference, within uncertainty, whether the forsterite dissolution rate was normalized to BET or the geometric surface area. As observed here, the calculated geometric surface area of forsterite was systematically greater (0.46 m^2) than that obtained from X-ray microtomography images and integrated over the entire flow-through reaction vessel (0.24–0.19 m^2). Using a fixed geometric surface for the calculations

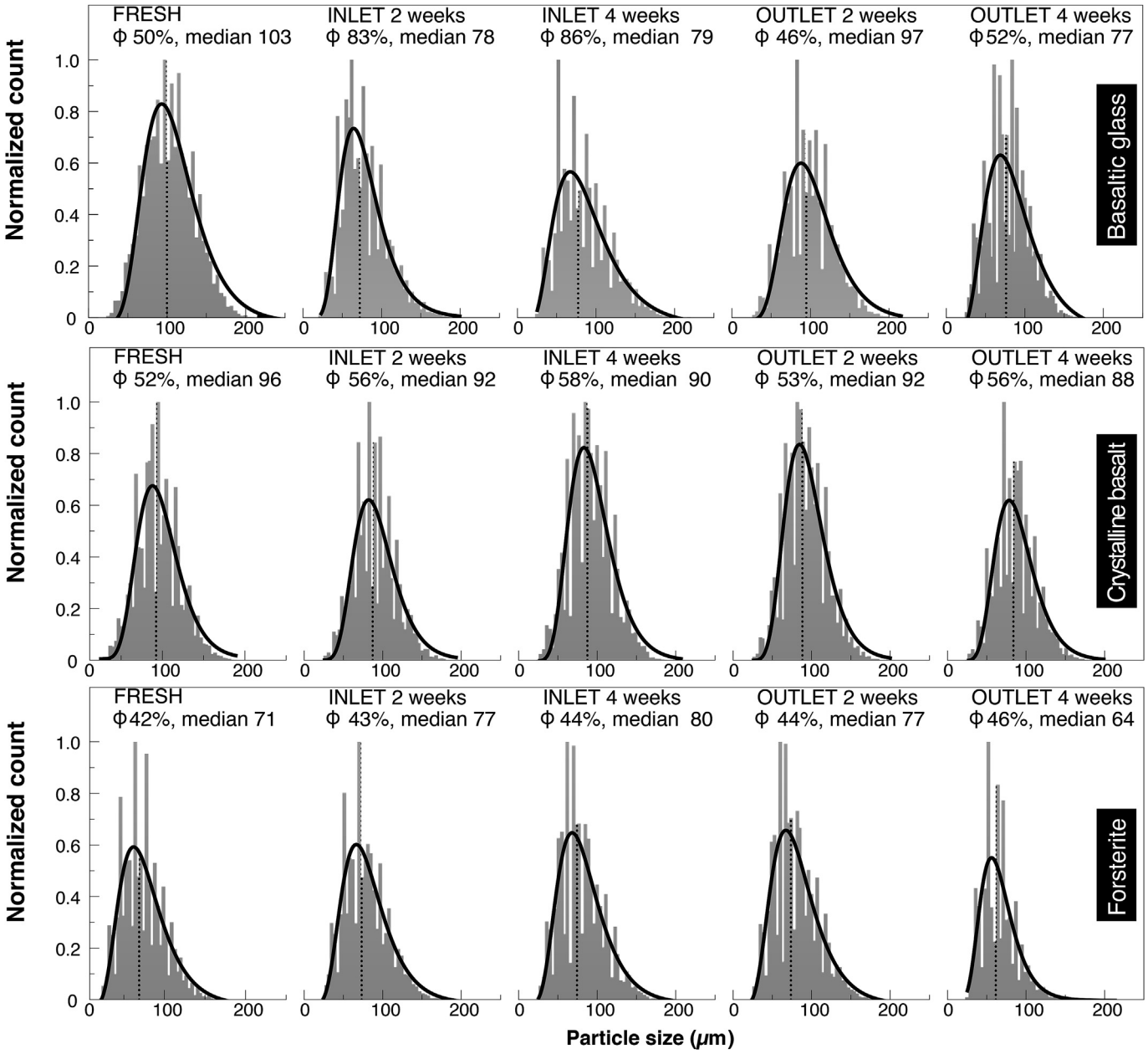

Fig. 6. Grain size distribution (lognormal) evolution as a function of time and distance in the reactor, determined from the 3D X-ray microtomography images. Porosity, ϕ, and median grain size are included.

resulted in lower reaction rates (log $r_{+,Si} = -7.52$ to -7.66 mol/m^2/s) whereas using the surface area obtained from the X-ray microtomography 3D images, which took into account the progressive decrease in forsterite surface, resulted in similar rates throughout the experiment (log $r_{+,Si} = -7.28$ to -7.24 mol/m^2/s).

For basaltic glass and crystalline basalt, the results were similar to forsterite. The rates determined from the geometric surface area were systematically lower than those determined from the X-ray microtomography measurements. Both the geometric and tomographic normalized rates obtained in this study compare well with those previously reported for crystalline basalt (Gudbrandsson et al., 2011) but the rate for basaltic glass was an order of magnitude lower than those reported by Gíslason and Oelkers (2003) (Table 7). The most probable reason was the different experimental setup, which resulted in a wide solute gradient with steeply increasing pH along our reaction pathway, which slowed the dissolution rate. The difference in surface area derived from the X-ray microtomography data was higher for basaltic glass and forsterite than for crystalline basalt, however the dissolution rate of crystalline basalt changed more during the experiment despite the changes in surface area.

From our results, we interpret that bulk dissolution rates for mafic minerals and rocks are relatively insensitive to change in the total surface area during progressive water-rock interaction. Dissolution of forsterite, basaltic glass and crystalline basalt all resulted in consumption of H^+ (acid) (reactions listed in Table 3), causing increased pH and decreased dissolution rates along the flow path. According to the geochemical model calculations, this was indeed to be expected, i.e. with increasing distance into the reactor, pH increases and dissolution rate decreases (Fig. 8). The

Table 6
The calculated rates of experimental dissolution using Si and Mg concentrations. The dissolution rates are normalized to geometric initial surface and tomographic surface. A_{XMT} tot = averaged surface area of tomographic measurements as a function of column distance, x, residual grams in the column (obtained from mass balance of outlet concentration).

Exp. #	Time days	A_{geo} tot m^2	A_{XMT} tot m^2	Dissolution rate, log $r_{+,i}$ (mol/m^2/s)			
				Si_{geo}	Si_{XMT}	Mg_{geo}	Mg_{XMT}
Basaltic glass							
BG 1 outlet	4	0.41	0.153	−7.57	−7.14	−7.27	−6.84
BG 2 outlet	6	0.41		−7.57		−7.30	
BG 3 outlet	8	0.41		−7.56		−7.30	
BG 4 outlet	10	0.41		−7.53		−7.30	
BG 5 outlet	15	0.41	0.144	−7.89	−7.44	−7.74	−7.28
BG 6 outlet	20	0.41		−7.77		−7.53	
BG 7 outlet	22	0.41		−7.68		−7.42	
BG 8 outlet	25	0.41		−7.59		−7.36	
BG 9 outlet	29	0.41	0.162	−7.58	−7.17	−7.37	−6.91
Average				−7.64 ± 0.12	−7.25 ± 0.22	−7.40 ± 0.15	−7.01 ± 0.25
Crystalline basalt							
XB 1 outlet	1	0.39	0.173	−8.07	−7.72	−7.36	−7.00
XB 2 outlet	3	0.39		−7.82		−7.02	
XB 3 outlet	6	0.39		−7.83		−7.02	
XB 4 outlet	9	0.39		−7.89		−7.09	
XB 5 outlet	11	0.39		−7.96		−7.20	
XB 6 outlet	13	0.39	0.166	−8.04	−7.68	−7.28	−6.91
XB 7 outlet	16	0.39		−8.18		−7.46	
XB 8 outlet	20	0.39		−8.26		−7.59	
XB 9 outlet	25	0.39		−8.40		−7.78	
XB 10 outlet	28	0.39		−8.45		−7.86	
XB 11 outlet	30	0.39	0.173	−8.45	−8.1	−7.91	−7.56
Average				−8.12 ± 0.24	−7.83 ± 0.23	−7.42 ± 0.33	−7.16 ± 0.35
Forsterite							
FO 1 outlet	1	0.46	0.238	−7.52	−7.24	−7.54	−7.26
FO 2 outlet	3	0.46		−7.54		−7.58	
FO 3 outlet	6	0.46		−7.58		−7.60	
FO 4 outlet	9	0.46		−7.61		−7.63	
FO 5 outlet	11	0.46		−7.55		−7.56	
FO 6 outlet	13	0.46		−7.58		−7.61	
FO 7 outlet	16	0.46	0.201	−7.63	−7.28	−7.66	−7.30
FO 8 outlet	20	0.46		−7.57		−7.60	
FO 9 outlet	28	0.46		−7.66		−7.69	
FO 10 outlet	30	0.46	0.186	−7.66	−7.27	−7.69	−7.30
Average				−7.59 ± 0.05	−7.26 ± 0.02	−7.62 ± 0.05	−7.29 ± 0.02

geometric dissolution rate from the inlet side of the reactor matched well with the results of Gíslason and Oelkers (2003). Increase of pH and decreasing rates in flow-through systems have been presented previously (Molins et al., 2014). The pH change from the inlet to the outlet of the column resulted in a corresponding dissolution decrease of 0.4–0.6 log units for the three solids studied. This was at a similar order and greater than the changes in the dissolution rate that resulted from changes in surface area at the inlet and outlet of the reactor and with time. It is therefore clear that small changes and heterogeneity in solution composition, including pH, can cause considerable effects on dissolution and the rate of elemental leaching.

4.2. Porosity and surface area change during progressive dissolution

During progressive mineral and rock dissolution, the porosity and surface area can change. In its simplest form, when only mineral dissolution occurs, mass decreases and pore volume increases. The specific surface area for individual grains increases due to reduction in grain size; the overall specific surface area of the material may change differently as small particles may also dissolve to completion, leaving a residue with, on average, larger particles. In more complex cases, progressive water-rock interaction dissolves primary solid phases and forms secondary phases. This can result in solid volume increase if the mole volume of the secondary phases is greater than the mole volume of the primary phases initially. An example is calcium carbonate precipitation experiments in cylindrical plug flow column reactors filled with calcite seed and glass beads (Noiriel et al., 2012, 2015). As a result, porosity can decrease in the rock matrix because of progressive water-rock interaction. In this work, we focused on the simpler case, dissolution only.

The changes in porosity were determined for the inlet and outlet sides of the flow-through reactor column using in situ XMT images. Progressive mineral and rock dissolution caused porosity in the columns to increase. Changes were greatest for basaltic glass, followed by crystalline basalt and forsterite (Fig. 9). Preferential dissolution was observed on the inlet side of the flow-through reactor. This trend was consistent with predictions from the reactive transport modeling, with dissolution of basaltic glass leading to pore volume increase from 50 to 90% on the inlet side but only 60% at the outlet side after 4 weeks of dissolution. These differences within the flow-through reactor system resulted from the pH dependence of the mineral and rock dissolution rates on progressive consumption of H^+ from the solution, increasing the pH and slowing the dissolution rate (Fig. 8). The average final porosity derived from the modeling matched well with the averaged XMT porosity for the glass (4% difference) and crystalline basalt (3% difference) but for olivine, the difference derived from solution composition was 27% higher. The reason for these differences was a different solid mass used for different experiments and the olivine

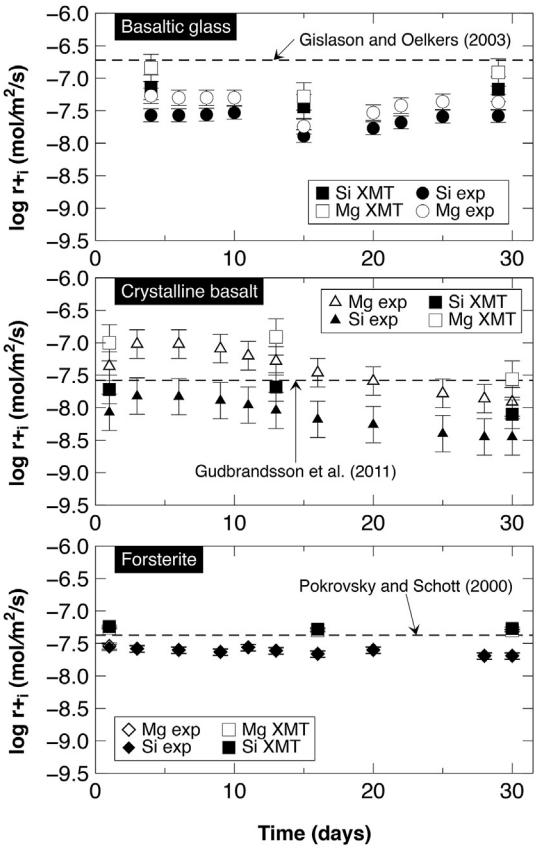

Fig. 7. Dissolution rates based on Si and Mg solution concentration as a function of time. The rates have been normalized to bulk geometric surface area (exp) or to the surface area derived from the X-ray microtomography images (XMT). The lines represent geometric normalized Si rates from the literature, recalculated for pH averaged from the experiments.

was finer grained than the basaltic glass or the crystalline basalt. The finest material dissolved first and its loss had no major impact on porosity (Fig. 9). The columns containing crystalline basalt and amorphous glass had similar initial porosity and grain size. The glass dissolved faster and its porosity changed heterogeneously compared with the less reactive crystalline basalt, which dissolved more homogeneously, as predicted by the spherical and sugar cube dissolution modeling.

Progressive mineral and rock dissolution decreases grain size and this was observed by XMT and geochemical modeling. Surface area increased as water-rock interaction progressed. The changes were reasonably modeled by the reactive transport simulations, particularly in the case of basaltic glass, but less successfully for forsterite and crystalline basalt (Fig. 10). Very little difference resulted from the method used for calculating surface area, i.e. the sugar lump or the spherical loss approach.

4.3. Do geochemical model calculations predict reactive transport behavior in porous media?

Reactive transport models are used to understand: the composition of natural waters; acidic water generation and leaching of metals from mine wastes; the origin of mineral deposits; the formation and dissolution of rocks and minerals in geologic formations in response to re-injection of industrial wastes, steam, CO_2 and H_2S; and to predict contaminant plume migration such as radionuclides in waste repositories, biodegradation of chemicals in landfills, and other contaminants (e.g., Steefel et al., 2005).

Comparison of the results from the reactive transport modeling and the experimental observations for solution composition, porosity, and surface area evolution for mineral and rock dissolution in a flowing system revealed some important aspects in the capabilities and limitations of commonly applied reactive transport modeling. First, some of the studied minerals and rocks were not observed to dissolve stoichiometrically. Non-stoichiometric dissolution of minerals and solids is usually not taken into account in geochemical modeling. However, such a modeling approach is possible by redefining individual elemental leaching rates along the flow-path and time rather than bulk mineral or solid dissolution rate. Second, fluid dynamics and preferential flow are commonly ignored in simple reactive transport modeling. This however affects the pore fluid composition and in turn the dissolution rates and changes in pore volume and surface area with time. Faster refill rate of the solution and/or a higher water/rock ratio would enhance the dissolution and porosity generation. However, the capacity of the model to infer the dissolution dynamics at larger field scales is not affected when the same macroscopic approach is applied to define input parameters as presented here in the models. Moreover, the systems under study were the simplest cases: dissolution far from equilibrium. For systems at close-to-equilibrium, other complications can be introduced like nucleation and growth of secondary phases; flow path heterogeneity favouring non-uniform precipitation patterns; and geometry of porous network and in turn

Table 7
Comparision of dissolution rates obtained in this study and reported in the literature.

Solid	pH/25 °C	Surface area	log $r_{+,Si}$ mol/m^2/s	Reference
Basaltic glass	2.25–2.92	geo	−7.64 ± 0.12	This study
	2.25–2.92	XMT	−7.25 ± 0.22	This study
	2.50	geo	−6.34[a]	Gíslason and Oelkers (2003)
Crystalline basalt	2.19–2.34	geo	−8.12 ± 0.24	This study
	2.19–2.34	XMT	−7.83 ± 0.23	This study
	2.30	geo	−7.64[a,b]	Gudbrandsson et al. (2011)
Forsterite	2.48–2.86	geo	−7.59 ± 0.05	This study
Forsterite	2.48–2.86	XMT	−7.26 ± 0.02	This study
Forsterite	2.62	geo	−7.66	Olsen and Rimstidt (2008)
Forsterite	2.00	geo	−6.97[a]	Oelkers (2001)
Forsterite	3.05	geo	−7.58 [a]	Golubev et al. (2005)
Forsterite	2.50	geo	−7.46	Rimstidt et al. (2012)
Forsterite	2.70	geo	−7.23[a]	Pokrovsky and Schott (2000)

[a] Converted to geo from BET surface area.
[b] Extrapolated.

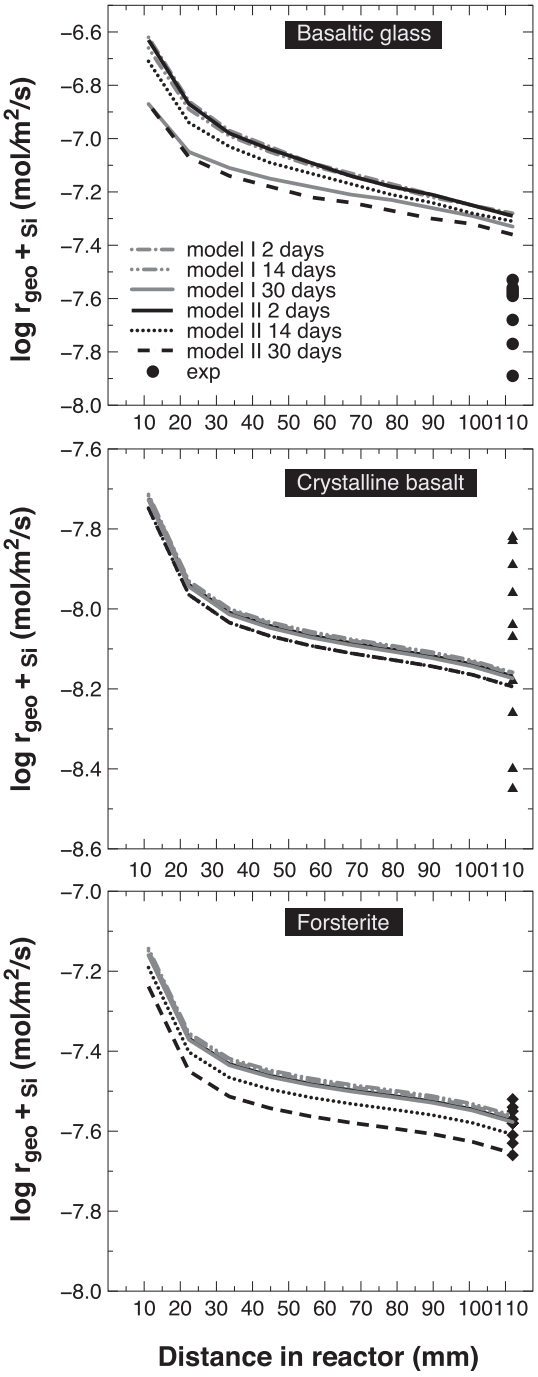

Fig. 8. Dissolution rates derived from the reactive transport modeling as a function of distance through the reactor. Model I used the sugar lump approach to estimate change in surface area (gray) and Model II assumed spherical particles with homogeneous loss (black).

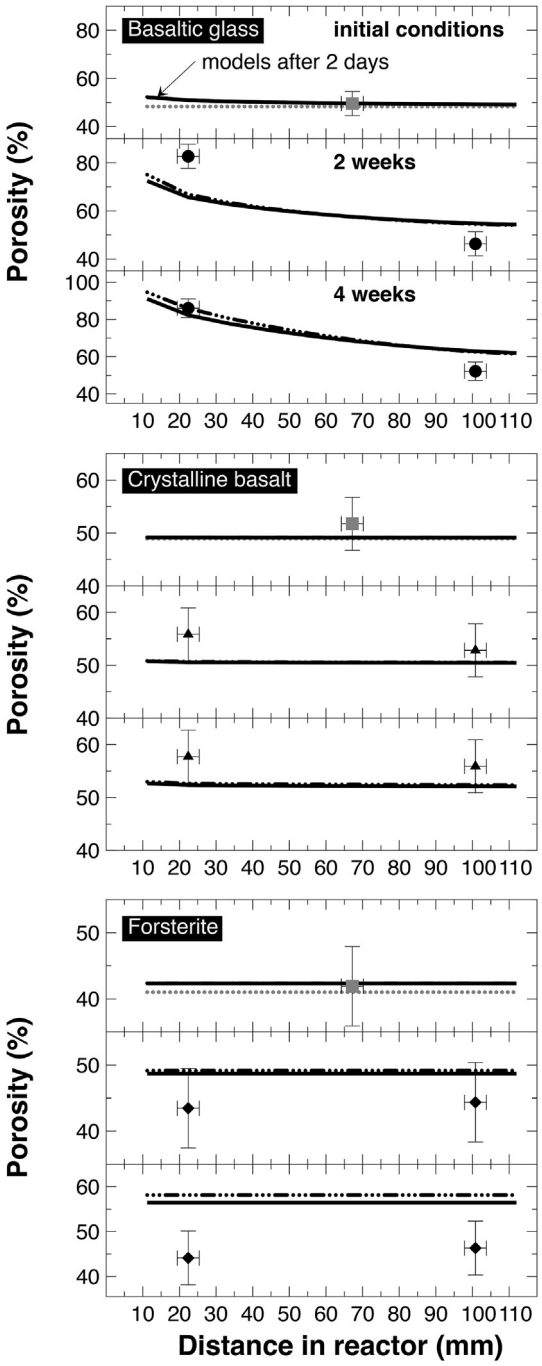

Fig. 9. Experiment (symbols) and model derived (lines) porosity as a function of distance at initial conditions (gray square and gray line marked), 2 and 4 weeks of interaction. The model that used simple spherical dissolution is the solid line, the model that used sugar lump dissolution is shown as a dashed black line.

closure of flow paths with time (Noiriel et al., 2015; Peuble et al., 2015). Third, similar results were obtained for mineral surface area and surface area normalized dissolution rates independent of the method applied in the calculations, i.e. whether geometric or tomographic normalized surface area was used for calculating solid dissolution rates or whether the simple spherical model or the more complicated sugar lump model was used. Fourth, the dissolution rates obtained from a complex flow-through system were observed to be comparable to those obtained from mixed flow reactor experiments at far from equilibrium. However, observed differences in our results arose from changes in the properties of the solid and solution along the flow path and as a function of time, such as surface area heterogeneity and pH variations. Such variations must be included in computations to be able to compare the two systems. Fifth, the calculated porosity and surface area changes along flow-path and time were observed to represent similar trends as those measured, however, accurate values are difficult to predict. This points towards the problem of the predicting capabilities of reactive transport modeling, i.e. calculations of pore

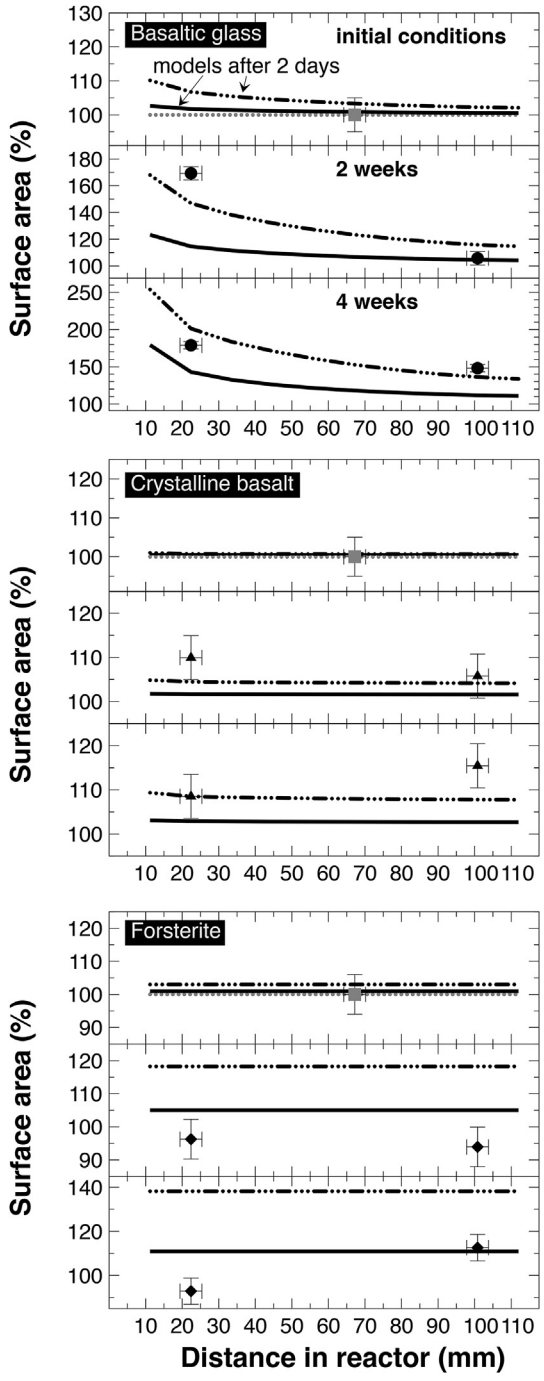

Fig. 10. Experiment (symbols) and model derived (lines) specific surface area as a function of distance at initial conditions (gray square and gray line marked), 2 and 4 weeks of interaction converted to % = $\frac{surface\ at\ time}{initial\ surface}$*100. The model with simple spherical dissolution is represented with a full line; the model that uses sugar lump dissolution is shown as a dashed black line.

volume and mineral and rock surface area changes with time and along flow paths that in turn are key parameters in determining dissolution rates, overall chemical mass movement in the system, and fluid flow paths and velocities.

5. Conclusions

Mineral and rock dissolution was studied experimentally using flow-through reactors and reactive transport modeling. The studied rocks and minerals were forsterite and crystalline and amorphous basalt, dissolved in HCl solutions at pH ~2.5. Solution composition, particle surface area, and porosity were determined as a function of reaction time and travel distance within the reactor, using in situ X-ray computed tomography (XMT) and chemical composition of the inlet and outlet solutions. Comparison of the results from the modeling and experiments demonstrate some important points.

(1) The dissolution rates far from equilibrium obtained here using a complex flow-through system were observed to be comparable to those obtained from mixed flow reactor experiments. The rates, normalized to the initial geometric surface area, were: log $r_{+,Si}$ −7.59 ± 0.05 for forsterite, −7.64 ± 0.12 for basaltic glass and −8.12 ± 0.24 (mol/m^2/s) for crystalline basalt, at 25 °C and pH ~2.5.
(2) Some of the minerals and rocks were not observed to dissolve stoichiometrically; such non-stoichiometric dissolution of minerals and solids is commonly not taken into account in reactive transport modeling.
(3) Similar results were obtained independent of the method applied in the calculations for mineral surface area and surface area normalized dissolution rates, i.e. whether geometric or tomographic normalized surface area was used or whether the simple spherical model or more complicated sugar lump model implemented.
(4) Mineral and rock dissolution resulted in increased porosity and specific surface area of the solids; these changes were not uniformly distributed along the fluid flow path or with time. Similar trends were predicted by reactive transport modeling, however, true values were difficult to predict. It follows that accurate prediction capabilities of simple reactive transport modeling may be limited for calculating pore volume and mineral and rock surface area changes with time and along flow paths that in turn are key parameters in determining dissolution rates, overall chemical mass movement in the system, and fluid flow paths and velocities.

Acknowledgements

We thank Gissur Örlygsson, Nicole Keller, Matthijs A. Smith, Snorri Guðbrandsson and Prathap Moola for analytical and experimental assistance. We also thank two anonymous reviewers for providing insightful reviews on the original manuscript and Michael Kersten for editorial handling. This research was made possible by a Marie Curie grant from the European Commission in the 7th Framework, as the MINSC ITN (Initial Training Research Network) Project Number 290040, and Landsvirkjun grant DOK-08-2016 to J. Přikryl.

References

Aagaard, P., Helgeson, H.C., 1982. Thermodynamic and kinetic constraints on reaction rates among minerals and aqueous solutions: I. Theoretical considerations. Am. J. Sci. 282, 237–285.
Akcil, A., Koldas, S., 2006. Acid mine drainage (AMD): causes, treatment and case studies. J. Clean. Prod. 14, 1139–1145.
Appelo, C.A.J., Postma, D., 2005. Geochemistry, Groundwater and Pollution. CRC Press.
Aradóttir, E.S.P., Sonnenthal, E.L., Jónsson, H., 2012. Development and evaluation of a thermodynamic dataset for phases of interest in CO_2 mineral sequestration in basaltic rocks. Chem. Geol. 304, 26–38.
Aradóttir, E.S.P., Sigfússon, B., Sonnenthal, E.L., Björnsson, G., Jónsson, H., 2013. Dynamics of basaltic glass dissolution–Capturing microscopic effects in continuum scale models. Geochim. Cosmochim. Acta. 121, 311–327.
Arnórsson, S., Andrésdóttir, A., 1999. The Dissociation Constants of Al-hydroxy Complexes at 0–350°C and Psat. Geochemistry of the Earth's Surface, Balkema, Rotterdam, pp. 425–428.
Arnórsson, S., Stefánsson, A., 1999. Assessment of feldspar solubility constants in water in the range 0° to 350°C at vapor saturation pressures. Am. J. Sci. 299,

173–209.
Brantley, S.L., Kubicki, J.D., White, A.F., 2008. Kinetics of Water-rock Interaction. Springer, New York.
Brantley, S.L., Mellott, N.P., 2000. Surface area and porosity of primary silicate minerals. Am. Mineral. 85, 1767–1783.
Brueckner, H.K., Carswell, D.A., Griffin, W.L., Medaris, L.G., Van Roermund, H.L.M., Cuthbert, S.J., 2010. The mantle and crustal evolution of two garnet peridotite suites from the Western Gneiss Region, Norwegian Caledonides: an isotopic investigation. Lithos 117, 1–19.
Cnudde, V., Boone, M.N., 2013. High-resolution X-ray computed tomography in geosciences: a review of the current technology and applications. Earth-Sci. Rev. 123, 1–17.
Colón, C.F.J., Oelkers, E.H., Schott, J., 2004. Experimental investigation of the effect of dissolution on sandstone permeability, porosity, and reactive surface area. Geochim. Cosmochim. Acta. 68, 805–817.
Cox, J.D., Wagman, D.D., Medvedev, V.A., 1989. CODATA Key Values for Thermodynamics. Hemisphere Publication Corp.
Galeczka, I., Wolff-Boenisch, D., Oelkers, E.H., Gíslason, S.R., 2014. An experimental study of basaltic glass–H_2O–CO_2 interaction at 22 and 50°C: implications for subsurface storage of CO_2. Geochim. Cosmochim. Acta. 126, 123–145.
Gandy, C.J., Smith, J.W.N., Jarvis, A.P., 2007. Attenuation of mining-derived pollutants in the hyporheic zone: a review. Sci. Total Environ. 373, 435–446.
Giammar, D.E., Bruant, R.G., Peters, C.A., 2005. Forsterite dissolution and magnesite precipitation at conditions relevant for deep saline aquifer storage and sequestration of carbon dioxide. Chem. Geol. 217, 257–276.
Gíslason, S.R., Oelkers, E.H., 2003. Mechanism, rates, and consequences of basaltic glass dissolution: II. An experimental study of the dissolution rates of basaltic glass as a function of pH and temperature. Geochim. Cosmochim. Acta. 67, 3817–3832.
Gíslason, S.R., Oelkers, E.H., 2014. Carbon storage in basalt. Science 344, 373–374.
Golubev, S.V., Pokrovsky, O.S., Schott, J., 2005. Experimental determination of the effect of dissolved CO_2 on the dissolution kinetics of Mg and Ca silicates at 25°C. Chem. Geol. 217 (3), 227–238.
Gouze, P., Luquot, L., 2011. X-ray microtomography characterization of porosity, permeability and reactive surface changes during dissolution. J. Contam. Hydrol. 120–121, 45–55.
Gudbrandsson, S., Wolff-Boenisch, D., Gíslason, S.R., Oelkers, E.H., 2011. An experimental study of crystalline basalt dissolution from $2 \leq pH \leq 11$ and temperatures from 5 to 75°C. Geochim. Cosmochim. Acta. 75, 5496–5509.
Gudbrandsson, S., Wolff-Boenisch, D., Gíslason, S.R., Oelkers, E.H., 2014. Experimental determination of plagioclase dissolution rates as a function of its composition and pH at 22°C. Geochim. Cosmochim. Acta. 139, 154–172.
Gunnarsson, I., Arnórsson, S., 2000. Amorphous silica solubility and the thermodynamic properties of $H_4SiO^\circ_4$ in the range of 0° to 350°C at P_{sat}. Geochim. Cosmochim. Acta. 64, 2295–2307.
Gysi, A.P., Stefánsson, A., 2012a. CO_2-water–basalt interaction. Low temperature experiments and implications for CO_2 sequestration into basalts. Geochim. Cosmochim. Acta. 81, 129–152.
Gysi, A.P., Stefánsson, A., 2012b. Experiments and geochemical modeling of CO_2 sequestration during hydrothermal basalt alteration. Chem. Geol. 306–307, 10–28.
Gysi, A.P., Stefánsson, A., 2012c. Mineralogical aspects of CO_2 sequestration during hydrothermal basalt alteration — an experimental study at 75 to 250°C and elevated pCO_2. Chem. Geol. 306–307, 146–159.
Helgeson, H.C., Murphy, W.M., Aagaard, P., 1984. Thermodynamic and kinetic constraints on reaction rates among minerals and aqueous solutions. II. Rate constants, effective surface area, and the hydrolysis of feldspar. Geochim. Cosmochim. Acta. 48, 2405–2432.
Jha, D., Sørensen, H.O., Dobberschütz, S., Feidenhans'l, R., Stipp, S.L.S., 2014. Adaptive center determination for effective suppression of ring artifacts in tomography images. Appl. Phys. Lett. 105 (14), 143107–1-4.
Kieffer, B., Jové, C.F., Oelkers, E.H., Schott, J., 1999. An experimental study of the reactive surface area of the Fontainebleau sandstone as a function of porosity, permeability, and fluid flow rate. Geochim. Cosmochim. Acta. 63, 3525–3534.
Lichtner, P.C., 1996. Continuum formulation of multicomponent- multiphase reactive transport. Rev. Min. 34, 1–81.
Liu, X., Tanaka, M., Okutomi, M., 2013. Single-image noise level estimation for blind denoising. IEEE T. Image Process. 22 (12), 5226–5237.
Luquot, L., Gouze, P., 2009. Experimental determination of porosity and permeability changes induced by injection of CO_2 into carbonate rocks. Chem. Geol. 265, 148–159.
McGrail, B.P., Schaef, H.T., Ho, A.M., Chien, Y.J., Dooley, J.J., Davidson, C.L., 2006. Potential for carbon dioxide sequestration in flood basalts. J. Geophys. Res. 111.
Molins, S., Trebotich, D., Yang, L., Ajo-Franklin, J.B., Ligocki, T.J., Shen, C., Steefel, C.I., 2014. Pore-scale controls on calcite dissolution rates from flow-through laboratory and numerical experiments. Environ. Sci. Technol. 48, 7453–7460.
Nagy, K.L., Blum, A.E., Lasaga, A.C., 1991. Dissolution and precipitation kinetics of kaolinite at 80 degrees C and pH 3; the dependence on solution saturation state. Am. J. Sci. 291, 649–686.
Noiriel, C., Gouze, P., Bernard, D., 2004. Investigation of porosity and permeability effects from microstructure changes during limestone dissolution. Geophys. Res. Lett. 31.
Noiriel, C., Luquot, L., Madé, B., Raimbault, L., Gouze, P., van der Lee, J., 2009. Changes in reactive surface area during limestone dissolution: an experimental and modelling study. Chem. Geol. 265, 160–170.
Noiriel, C., Steefel, C.I., Yang, L., Ajo-Franklin, J., 2012. Upscaling calcium carbonate precipitation rates from pore to continuum scale. Chem. Geol. 318–319, 60–74.
Noiriel, C., 2015. Resolving time-dependent evolution of pore-scale structure, permeability and reactivity using x-ray microtomography. Rev. Min. Geochem. 80, 247–285.
Noiriel, C., Steefel, C.I., Yang, L., Bernard, D., 2015. Effects of pore-scale precipitation on permeability and flow. Adv. Water Resour. 95, 125–137.
Oelkers, E.H., 2001. An experimental study of forsterite dissolution rates as a function of temperature and aqueous Mg and Si concentrations. Chem. Geol. 175, 485–494.
Oelkers, E.H., Gíslason, S.R., 2001. The mechanism, rates and consequences of basaltic glass dissolution: I. An experimental study of the dissolution rates of basaltic glass as a function of aqueous Al, Si and oxalic acid concentration at 25°C and pH = 3 and 11. Geochim. Cosmochim. Acta. 65, 3671–3681.
Olsen, A.A., Rimstidt, J.D., 2008. Oxalate-promoted forsterite dissolution at low pH. Geochim. Cosmochim. Acta. 72, 1758–1766.
Otsu, N., 1979. Thresholds selection method form grey-level histograms. IEEE T. Syst. Man. Cyb. 9 (1), 62–66.
Palandri, J.L., Kharaka, Y.K., 2004. A Compilation of Rate Parameters of Water-mineral Interaction Kinetics for Application to Geochemical Modeling (No. Open-file-2004-1068). Geological Survey, Menlo Park CA.
Parkhurst, D.L., Appelo, C.A.J., 2013. Description of Input and Examples for PHREEQC Version 3—a Computer Program for Speciation, Batch-reaction, One-dimensional Transport, and Inverse Geochemical Calculations. U.S. Geological Survey Techniques and Methods, book 6.
Peuble, S., Godard, M., Luquot, L., Andreani, M., Martinez, I., Gouze, P., 2015. CO_2 geological storage in olivine rich basaltic aquifers: new insights from reactive-percolation experiments. Appl. Geochem. 52, 174–190.
Pokrovsky, O.S., Schott, J., 2000. Kinetics and mechanism of forsterite dissolution at 25°C and pH from 1 to 12. Geochim. Cosmochim. Acta. 64, 3313–3325.
Phillips, S.L., Hale, F.V., Silvester, L.F., Siegel, M.D., 1988. Thermodynamic Tables for Nuclear Waste Isolation: Vol. 1, Aqueous Solutions Database. Report LBL-22860, NUREG/CR-4864, SAND87–0323. Lawrence Berkeley Lab, Berkeley, CA, USA.
Rimstidt, J.D., Brantley, S.L., Olsen, A.A., 2012. Systematic review of forsterite dissolution rate data. Geochim. Cosmochim. Acta 99, 159–178.
Saldi, G.D., Jordan, G., Schott, J., Oelkers, E.H., 2009. Magnesite growth rates as a function of temperature and saturation state. Geochim. Cosmochim. Acta. 73, 5646–5657.
Shock, E.L., Helgeson, H.C., 1988. Calculation of the thermodynamic and transport properties of aqueous species at high temperatures and pressures: correlation algorithms for ionic species and equation of state predictions to 5kb and 1000°C. Geochim. Cosmochim. Acta. 52, 2009–2036.
Shock, E.L., Sassani, D.C., Willis, M., Sverjensky, D.A., 1997. Inorganic species in geologic fluids: correlations among standard molal thermodynamic properties of aqueous ions and hydroxide complexes. Geochim. Cosmochim. Acta. 61, 907–950.
Stefánsson, A., 2001. Dissolution of primary minerals of basalt in natural waters: I. Calculation of mineral solubilities from 0 C to 350 C. Chem. Geol. 172, 225–250.
Steefel, C.I., DePaolo, D.J., Lichtner, P.C., 2005. Reactive transport modeling: an essential tool and a new research approach for the Earth sciences. Earth Planet. Sci. Let. 240, 539–558.
Stockmann, G.J., Wolff-Boenisch, D., Gíslason, S.R., Oelkers, E.H., 2011. Do carbonate precipitates affect dissolution kinetics? 1: Basaltic glass. Chem. Geol. 284, 306–316.
Techer, I., Advocat, T., Lancelot, J., Liotard, J.M., 2001. Dissolution kinetics of basaltic glasses: control by solution chemistry and protective effect of the alteration film. Chem. Geol. 176, 235–263.
Tester, J.W., Worley, W.G., Robinson, B.A., Grigsby, C.O., Feerer, J.L., 1994. Correlating quartz dissolution kinetics in pure water from 25 to 625°C. Geochim. Cosmochim. Acta. 58, 2407–2420.
Tomasi, C., Manduchi, R., 1998, January. Bilateral filtering for gray and color images. In: Sixth International Conference on Computer Vision (IEEE Cat. No.98CH36271), Bombay, vol. 1998, pp. 839–846.
White, A.F., Brantley, S.L., 2003. The effect of time on the weathering of silicate minerals: why do weathering rates differ in the laboratory and field? Chem. Geol. 202, 479–506.